

Robust Nucleus Detection from Microscopical Image with Partially Labeled Exemplars

Linqing Feng, Jun Ho Song, Jiwon Kim, Soomin Jeong, Jin Sung Park, and Jinhyun Kim

Abstract—Quantitative analysis of cell nuclei in microscopic images is an essential yet still challenging source of biological and pathological information. The major challenge is accurate detection and segmentation of densely packed nuclei in images acquired under a variety of conditions. With sufficient training examples, Mask R-CNN-based methods have achieved state-of-the-art nucleus segmentation. However, the current pipeline requires fully annotated training images, which are time consuming to create and sometimes infeasible because of the noisy nature of microscopic images. Importantly, nuclei often have similar appearances within the same image; this similarity could be utilized to segment nuclei with only partially labeled training examples. We propose a simple yet effective region proposal module for the current Mask R-CNN pipeline to perform few-exemplar learning. To capture the similarities between the unlabeled regions and labeled nuclei, we apply decomposed self-attention to the learned features. On the self-attention map, we observe strong activation at the centers and edges of all nuclei, including the unlabeled ones. On this basis, our region proposal module propagates the partial annotations to the whole image and then proposes effective bounding boxes for the bounding box regression and binary mask generation modules. When trained with only 1/4 of the nuclei annotated, the baseline pipeline gives frequent false negatives, while our approach retains detection accuracy comparable to that of training with the fully annotated data. Moreover, our method can serve as a bootstrapping step to create a full annotation of a dataset, where annotations are iteratively generated and corrected until the predetermined coverage and accuracy are reached. The source code is available at <https://github.com/feng-lab/nuclei>.

Index Terms—nucleus segmentation, deep learning, convolutional neural networks, few-exemplar learning, computer-assisted annotating

I. INTRODUCTION

The cell nucleus is a fundamental biological structure containing important information, such as cell type, density, and viability. Automatically identifying and segmenting nuclei from microscopic images is the first step for many types of quantitative analyses with applications ranging from basic cell biology [1], [2] and systems neuroscience [3], [4] to cancer diagnosis [5]. This task is a challenging *instance*

segmentation task because it requires the correct detection of all instances of nuclei within an image along with precise labeling of the pixels belonging to each detected nucleus. Nucleus segmentation methods need to be instance aware to correctly separate touching nuclei. Meanwhile, such methods need to address difficulties such as high cell density, low contrast, intensity inhomogeneity, shape variation, weak boundaries, strong gradients inside the nucleus, and ambiguous overlapping.

Classical approaches, including thresholding [6]–[10], marker-controlled watershed [11]–[13], edge detection [14], shape matching [15]–[17] and region merging/growing [18]–[22], often assume a certain signal pattern of nuclei or cells, such as bright centers, strong boundaries or low signal gradients inside nuclei. These methods work well for certain datasets but tend to fail in difficult cases where the assumptions do not hold. Denoising and transformation [9], [13] could be used to improve these methods by creating transformed images that fit the assumptions more closely. Nevertheless, the applicability of such methods is limited by these assumptions.

On the other hand, machine learning-based approaches could learn nuclear signal patterns directly from labeled examples without any prior assumptions. Indeed, with sufficient training data, deep learning-based methods have dominated the nucleus segmentation task [23]. U-Net [24] and Mask R-CNN [25] are the two main deep learning frameworks used in nucleus segmentation. Both frameworks achieved top performance in Kaggle’s 2018 Data Science Bowl [26]–[29]. U-Net is a U-shaped convolutional network widely used in bioimage and medical image segmentation tasks. This network uses skip connections to combine features at different resolutions to generate accurate pixel-level predictions, but it is not instance aware. In order to adapt U-Net for instance segmentation, auxiliary tasks need to be added to learn features such as nuclei contours [30], overlapping borders [28], or within-nuclei locations [29], for separating touching nuclei instances. Then, some heavy postprocessing procedures are used to compose or fuse all pixel level predictions to produce segmentation of individual nuclei. Here, U-Net is used for pixel classification, and it has been shown that comparable performance can be achieved when using a stacked random forest classifier as the classification backend [31]. A mask region-based convolutional neural network (Mask R-CNN), on the other hand, is an instance-aware framework and directly operates on a single-nucleus level. This tool predicts bounding boxes for all nuclei in an image and then segments the nuclei inside the

This work was supported by the KIST Institutional Program (Project 2E27850) and the NRF Brain Research Program (NRF-2017M3C7A1043838). (Corresponding authors: Linqing Feng and Jinhyun Kim.)

L. Feng, J. Song, J. Kim, S. Jeong, J. Park, and J. Kim are with the Center for Functional Connectomics, Brain Science Institute, Korea Institute of Science and Technology (KIST), Seoul 02792, Korea (e-mail: feng@kist.re.kr, kimj@kist.re.kr).

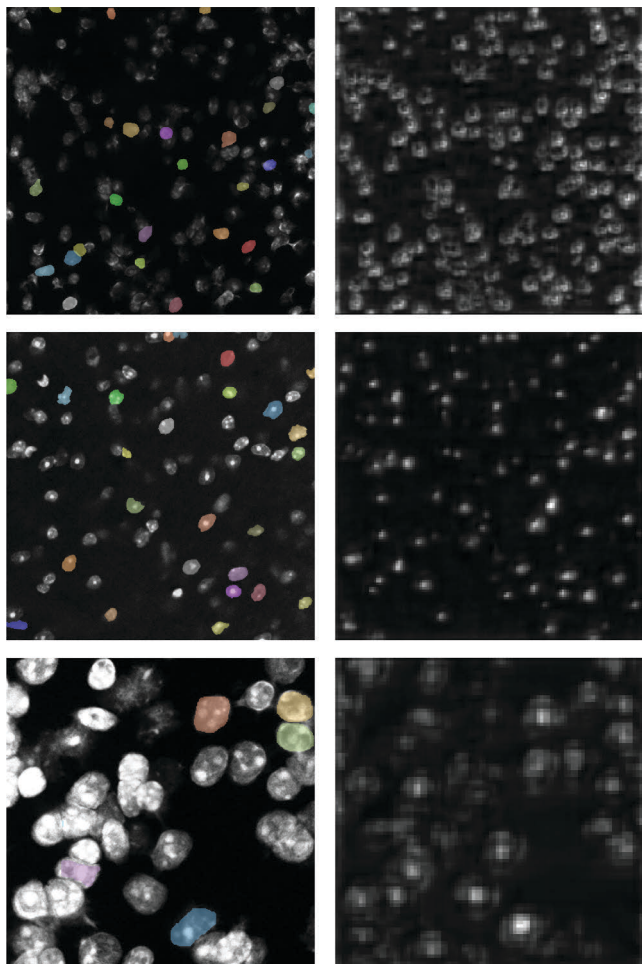


Fig. 1. An illustration of the learned attention maps. In each row, the first image shows an image of nuclei with a few color-coded annotations. The second image shows the merged attention map for the annotated (colored) regions. The self-attention module successfully models long-range correlation in images and generates meaningful attention focus, i.e., the centers and edges of nuclei.

predicted boxes. A Mask R-CNN can directly produce segmentation of individual nuclei and therefore requires little or no postprocessing [27]. Moreover, a Mask R-CNN can detect individual nuclei more accurately than U-Net [32] and has a simpler and more flexible framework.

Despite performing well, both deep learning frameworks require training images to be fully annotated [33]. Images of nuclei could be acquired under a variety of conditions and have varied appearance depending on the cell type, tissue preparation method, staining method, imaging modality and imaging parameters. When there are no publicly available annotated datasets for a certain type of nucleus image, it is very time consuming to create fully annotated images manually, especially if the nuclei are densely packed and depict ambiguous overlapping. In contrast, it is relatively easy and quick to label representative exemplars (i.e., partial labeling) in the image. In creating a fully annotated image, it is less labor intensive to refine or correct machine-generated annotations than to create annotations from scratch.

We extend the Mask R-CNN framework to robustly handle partially labeled training images. We adapt the self-attention mechanism [34], [35] to model long-range dependencies between nuclei. Inspired by the observed attention map (Figure 1), we built an additional module to predict the centers of nuclei and bounding boxes around the centers, effectively propagating the partial annotations to the whole image. The predicted bounding boxes, after non-maximum suppression, were merged with the other bounding box proposals generated by a Mask R-CNN and then sent to the standard bounding box regression and binary mask generation modules. We evaluated our method on a public dataset with $\frac{1}{4}$ of its original annotations. The results indicate that our method can handle partially labeled training datasets stably compared to the baseline framework while achieving a level of performance comparable to that of training with full annotation. We show that our method is also useful for generating full annotation for new datasets. The source code is available at <https://github.com/feng-lab/nuclei>.

II. METHODS

In the Mask R-CNN pipeline, the region proposal network (RPN) generates a large number of bounding box candidates (also named anchors) that densely cover the entire image and then calculates an objectness score for each candidate, which indicates the probability of this candidate containing a nucleus. During training, all bounding box candidates are matched to the ground-truth nucleus bounding boxes. Candidates that have a large intersection over union (IoU), i.e., high overlap ratio, with any ground-truth box are considered positive samples and have an objectness score of 1, whereas candidates that have low IoU values with all ground-truth boxes are considered negative samples and have an objectness score of 0. The RPN learns to calculate the objectness score by sampling positive and negative boxes and then computing the cross-entropy loss. The RPN selects and refines bounding box candidates with high objectness scores and then sends those selected to the region convolutional network (R-CNN). The R-CNN further evaluates the objectness of the selected candidates with more relevant features, using a similar strategy to RPN to sample positive and negative boxes. If the training dataset is only partially labeled, the pipeline cannot sample negative boxes correctly because a candidate box might contain an unlabeled nucleus but have low IoU with all labeled nuclei. These false negatives, if sampled by an RPN or R-CNN, could potentially impair the discrimination ability of the network and cause low detection recall. Therefore, we build a module to detect the bounding boxes of all potential nuclei in an image based on their similarity with the labeled ones. The detected boxes serve two purposes: 1) during training, they are used to prevent RPN and R-CNN from sampling false negative boxes; 2) during inference, they are used as “strong” proposals to improve the detection recall.

We used the self-attention mechanism [34] to capture the similarity between nuclei. The self-attention module calculates response at a position as a weighted sum of the features at all positions, thereby efficiently modeling long-range correlations. The self-attention mechanism has improved the performance of convolutional networks on many vision tasks, including

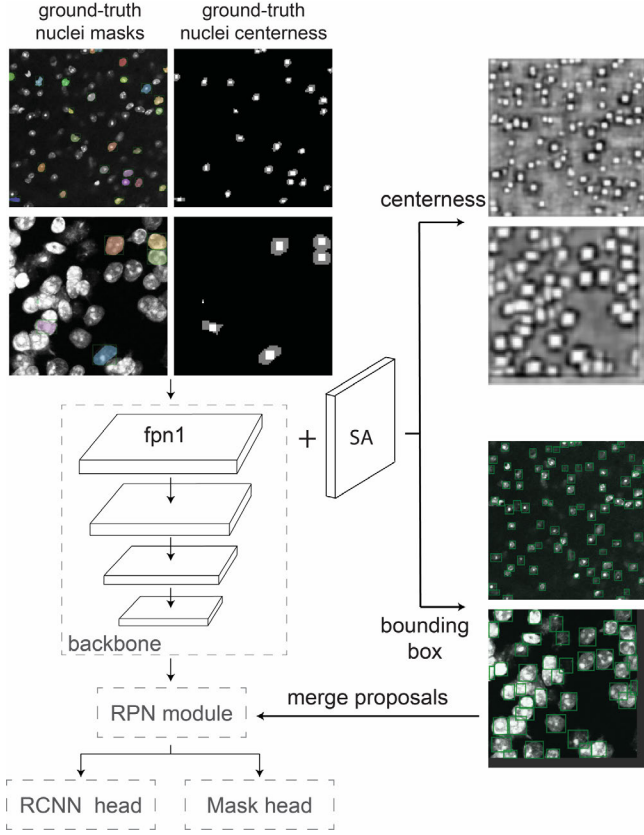


Fig. 2. **The proposed pipeline for learning from partially labeled exemplars.** With only partially labeled ground-truth, we design a task to learn and predict a centerness score and a bounding box for each spatial location of fpn1, the first feature level of the backbone network. The predicted bounding boxes capture most of the nuclei in image and are used to improve training and inference. Backbone, RPN module, RCNN head, and Mask head are standard Mask R-CNN components. SA is the decomposed self-attention module.

instance segmentation. We adopted the decomposed self-attention module [35] because it is more memory-efficient for handling large images. Specifically, for image features x with C channels and N spatial locations ($x \in R^{C \times N}$), the decomposed self-attention enhanced feature is calculated as $x_{att} = x + W_f((S(W_b x, C)(W_v x)^T)^T S(W_c x, N))$, where $W_f \in R^{C \times C_v}$, $W_c \in R^{C_b \times C}$, $W_b \in R^{C_b \times C}$, and $W_v \in R^{C_v \times C}$ are parameter matrices implemented as 1×1 convolutions. Here, $S(W_b x, C)$ indicates channelwise softmax normalization, and $S(W_c x, N)$ indicates locationwise softmax normalization. C_b and C_v are channel counts of the basis and value, respectively. We use $C_b = C_v = 64$ in all our experiments. Figure 1 shows the visualization of the attention map on the first-level feature of the feature pyramid network (fpn1) [36]. When we query the attention focus of the labeled nuclei, the self-attention module successfully captures the semantically related regions (i.e., all nuclei in the image) and generates meaningful focus on the centers and edges of nuclei.

Inspired by the attention map, we build a simple partial annotation handling module to predict nuclei centers and

bounding boxes around centers. Figure 2 illustrates the architecture of the Mask R-CNN with the proposed module. In brief, the Mask R-CNN is composed of a backbone network for generating multiscale features, an RPN module for generating bounding box proposals, an R-CNN head for evaluating and refining bounding box proposals, and a Mask head for generating binary masks, which in this case are the segmentations of all nuclei. Our proposed module uses the fpn1 feature because it has the highest spatial resolution among the features generated by the backbone network. It predicts the probability of being the center of a nucleus (i.e., centerness score) at each spatial location of fpn1 and, for each nucleus center, a 4-dimensional bounding box regression result.

Given a labeled nucleus instance with binary mask M and bounding box $b = [x_c, y_c, w, h]$, where (x_c, y_c) is the center of the box and w, h are box width and height, respectively. We project both its binary mask and bounding box to fpn1 and obtain the projected (downsampled) binary mask M^p and bounding box $b^p = [x_c^p, y_c^p, w^p, h^p]$. We define the center of the nucleus bounding box as $b_c^p = [x_c^p, y_c^p, 0.3 \times w^p, 0.3 \times h^p]$. In the ground-truth nucleus centerness map, we assign all pixels in b_c^p to one (positive), assign all pixels in M^p but not in b_c^p to zero (negative), and assign all other pixels to -1 (ignored). Examples of ground-truth nucleus centerness maps are illustrated in Figure 2 top. Positive, negative, and ignored pixels are shown in white, gray and black, respectively. For each positive pixel location l^p with ground-truth bounding box b , we empirically create an anchor bounding box $b_a = [x_l, y_l, \bar{w}, \bar{h}]$, where (x_l, y_l) is the coordinate of l^p in image space and \bar{w}, \bar{h} are median box width and height in training dataset, respectively.

During training, we randomly sample 512 pixels in the ground-truth nuclei center map to compute the cross-entropy loss $L_{centerness}$ of a batch, where the sampled positive and negative pixels have a ratio of up to 1:1. For the sampled positive pixels, we use the smooth L_1 loss defined in [37] to calculate their bounding box regression loss $L_{centerbox}$. The overall loss used in training is $L = L_{centerness} + L_{centerbox} + L_{maskrcnn}$, where $L_{maskrcnn}$ is the loss used in the original Mask R-CNN pipeline.

The centerness score and bounding boxes predicted by our module can be visualized in the right bottom of Figure 2. To obtain the predicted bounding boxes, we binarize the predicted centerness map with a threshold of 0.95. Then, for each connected component in the binarized centerness map, we choose the pixel with the highest centerness score and generate its bounding box by using its anchor bounding box and the regression result. During training, the predicted bounding boxes are sent to the RPN and the R-CNN head to prevent them from sampling false negatives during loss calculation. During inference, the predicted bounding boxes are treated as “high score” candidates and are directly sent to R-CNN for refinement.

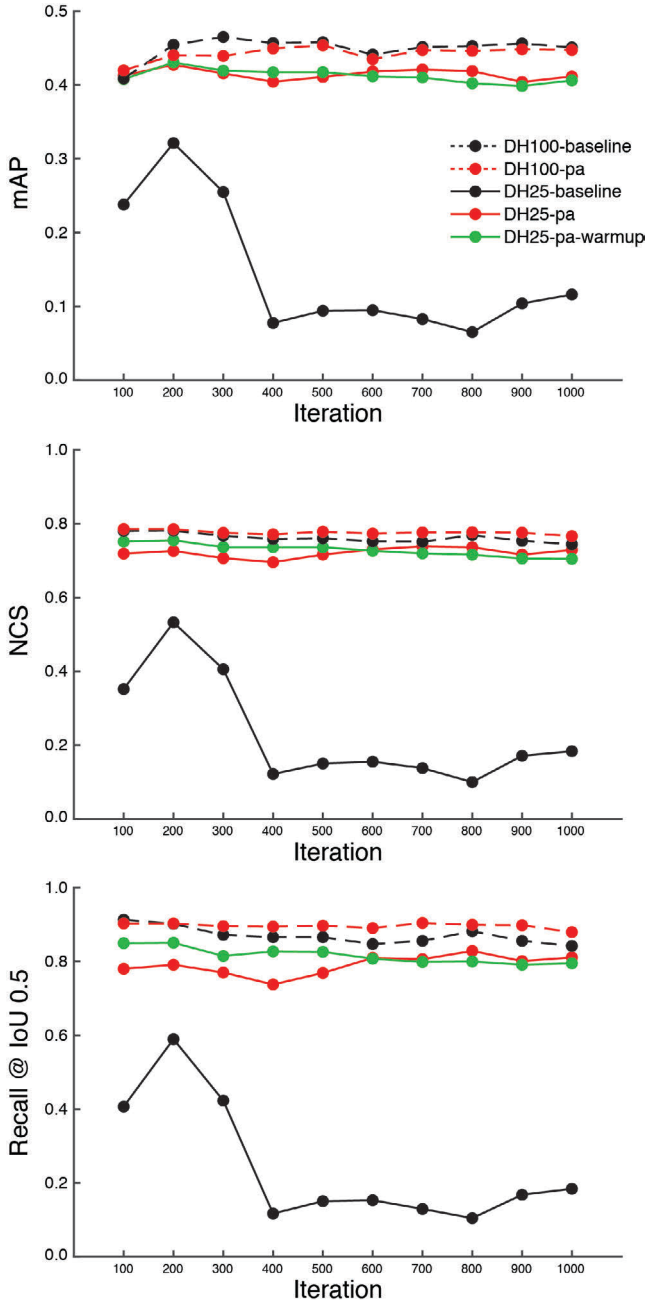


Fig. 3. The performance of all models measured by mAP, NCS, and recall at IoU of 0.5.

III. RESULTS

We evaluated the proposed method on the nucleus dataset published in [31]. The dataset is fully annotated, and we refer to it here as DH100. To create a partially labeled dataset, we randomly removed 75% of the annotations from the training set and named the resulting dataset DH25. DH100 contains 60

images with 2120 nuclei annotations, while DH25 contains the same 60 images with 525 annotations. An example training image of DH25 with annotations is shown in the bottom left of Figure 1. The baseline is a Mask R-CNN with a ResNeXt-101-64x4d backbone [38]. We trained the baseline model and our proposed model on both DH100 and DH25 and then evaluated their performance on the fully annotated test set, which contains 23 images with 951 nuclei annotations. We initialized all models with the weights of the model pretrained on the MS-COCO dataset. All models were trained for 1000 iterations on 4 NVIDIA Tesla V100 graphics processing units (GPUs). The batch size was 8. We use a fixed learning rate of 0.01 with weight decay and gradient norm clipping. No image augmentation was used except for vertical and horizontal flipping. For postprocessing, we simply dilated the detected nuclei with a rectangular structuring element of size 3×3 , as suggested by [27]. Other hyperparameters followed the latest release of the Mask R-CNN benchmark [39].

A. Evaluation

Mean average precision (mAP) was used as the evaluation metric in the Kaggle competition [26]. mAP is the mean average precision at different thresholds of the IoU between the ground truth and predicted segmentation and is calculated as

$$\frac{1}{|\text{thresholds}|} \sum_{t=0.5:0.05:0.95} \frac{TP(t)}{TP(t) + FP(t) + FN(t)}$$

where t is the IoU threshold, TP, FP, and FN are true positives, false positives, and false negatives, respectively. Normalized coverage score (NCS) values were used in [31] to evaluate the matching quality between ground truth and predicted segmentation. NCS is defined as

$$\text{NCS} = \frac{1}{\sum_{j=1}^{|G|} |r_j^G|} \sum_{j=1}^{|G|} |r_j^G| \max_{k=1, \dots, |S|} \text{IoU}(r_j^G, r_k^S)$$

where r^G is the ground truth, r^S is the predicted segmentation, $|G|$ is the number of ground-truth nuclei, and $|S|$ is the number of predicted nuclei. We report both mAP and NCS along with the recall at an IoU of 0.5.

B. Overall Performance

We refer to the baseline Mask R-CNN model as “DH100-baseline” or “DH25-baseline”, depending on the training dataset. Similarly, we refer to our model, which is the baseline Mask R-CNN plus our partial annotation handling module, as “DH100-pa” or “DH25-pa”. To examine the performance dynamics of these models as training progresses, we evaluated their performance every 100 iterations, which is approximately 13 epochs for this dataset. Figure 3 shows the performance of all models measured by mAP, NCS, and recall at an IoU of 0.5.

In Figure 3, we can see that the baseline model does not work well on the partially labeled training set (“DH25-baseline”). This outcome is not unexpected because the baseline model has

an implicit assumption that the input ground truth should contain all nuclei. Compared to the baseline model trained on the full dataset (“DH100-baseline”), “DH25-baseline” shows obviously decreased NCS and recall. Meanwhile, the detection precision of the model, measured as $TP/(TP + FP)$, is not greatly affected (data not shown). This observation is consistent with our previous analysis that sampling false negatives during training will cause low recall. The performance of “DH25-baseline” peaks at the beginning stage, then deteriorates as the network samples more and more false negatives.

In contrast, our model “DH25-pa” shows comparable performance to “DH100-pa”, despite being trained with fewer annotations. This performance demonstrates that our proposed module can alleviate the aforementioned false negative sampling problem and thus help the network learn from the partially annotated dataset. Additionally, note that the recall rate (as well as the NCS) of “DH25-pa” increases as the training progresses, indicating that our proposed module gradually learns to detect increasing numbers of nuclei in the unlabeled regions.

Although our model is designed to handle partially annotated datasets, it does not degrade the performance of the baseline framework when used with a fully annotated dataset. As shown in Figure 3, the “DH100-pa” model has close performance to “DH100-baseline”. The former also shows slightly superior performance in terms of NCS and recall, indicating that the module we added can generate high-quality nucleus proposals, which could potentially be used to further improve the detection framework.

We summarize the best mAP for each model, along with the corresponding iteration counts and other metrics in Table I. With the pretrained MS-COCO model as the starting point, all models can quickly adapt to the nuclei detection task and converge to an optimal state in a few iterations. Models trained on DH100 take more iterations than models trained on DH25 to reach peak performance because they are trained on more annotations. Furthermore, all of our models, even those trained with fewer annotations, show better NCS performance than those (approximately 0.6) reported in [31].

C. Training Strategy

In the previous setting, we trained our partial annotation handling module together with other components of the Mask R-CNN, namely, the RPN, R-CNN head and Mask head. One of the main functions of our partial annotation handling module is to predict the locations of all nuclei and prevent the RPN and R-CNN head from sampling false negatives. However, at the beginning stage of training, our partial annotation handling module could not yet recognize all nuclei in the image; therefore, the RPN and R-CNN head will inevitably sample some false negatives. These false negatives could potentially degrade the performance of the network, especially its recall rate. Indeed, we can see in Table I that the gap between recall of “DH25-pa” and “DH100-baseline” is larger than that of other metrics. The gradually increasing recall rate of “DH25-pa” in Figure 3 also indicates that the partial annotation handling module requires many iterations to reach an optimal state. To

TABLE I
BEST EVALUATION PERFORMANCE OF EACH MODEL

Model	mAP	NCS	Recall (IoU 0.5)	Iteration
DH100-baseline	0.465	0.767	0.871	300
DH100-pa	0.454	0.778	0.897	500
DH25-baseline	0.321	0.533	0.590	200
DH25-pa	0.427	0.726	0.791	200
DH25-pa-warmup	0.431	0.755	0.851	200

Best evaluation scores on each dataset are indicated by bold texts.

TABLE II
PERFORMANCE OF DIFFERENT METHODS ON THE HISTOPATHOLOGY TEST IMAGES

Method	Annotation Type	No. of Annotations	AJI
CNN3 [40]	full	13,372	0.5385
DIST [33]	full	5,577	0.5853
ours	partial	1,425	0.5335

address this problem, we started by training our partial annotation handling module alone for 500 iterations and then trained the whole network together. The model trained with this strategy was designated “DH25-pa-warmup”. Meanwhile, the overall performance of this model is more or less consistent with that of “DH25-pa” (Figure 3), showing that the whole framework is robust for end-to-end joint (partial annotation handling and other components of the Mask R-CNN) training. This strategy consistently improves the peak model performance (Table I) and further reduces the performance gap between training with partial annotation DH25 and training with full annotation DH100 at the price of slightly longer training time.

D. Histopathology Images

To demonstrate the generality of our method, we evaluated it on hematoxylin and eosin (H&E)-stained histopathology datasets presented in [33] and [40]. The top-performing model for breast cancer samples in [33] used 54 images (4 of which come from [40]) for training and 2 images from [40] for testing. The training images contained 5577 fully annotated nuclei, and the testing images contained 710 nuclei. We used the same training images here, except that we randomly removed 75% of the annotations from the training set so that our method is trained with only 1425 partially annotated nuclei. We trained our network for 200 iterations after a 1000-iteration warmup. The warmup stage was extended compared to the training for DH25 because this dataset contains additional nuclei annotations. To compare the performance of our method with the methods presented in [33] and [40], we performed inference on the test set and evaluated the accuracy with the aggregated Jaccard index (AJI). Formally, AJI is defined as

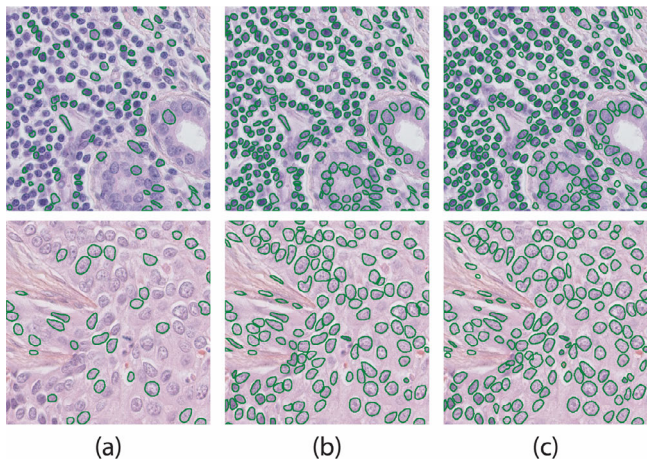


Fig. 4. Results on histopathology images show that our method successfully propagate partial annotations to the whole image. (a) Annotations used for training. (b) Ground truth. (c) Nuclei predicted by our method.

$$AJI = \frac{\sum_{j=1}^{|G|} |r_j^G \cap r_*^S(j)|}{\sum_{j=1}^{|G|} |r_j^G \cup r_*^S(j)| + \sum_{l \in U} |r_l^S|}$$

, where r^G represents ground truth, r^S is the predicted segmentation, $|G|$ is the number of ground-truth nuclei, $r_*^S(j)$ is the predicted nucleus that maximizes the IoU with ground truth r_j^G (with $r_*^S(i) \neq r_*^S(j)$ for $i \neq j$), and U is the set of predicted nuclei that are not matched to any ground truth. AJI is similar to NCS except that it also punishes detections that are not matched to ground truth. The results are shown in Table II. Compared to the methods that use full annotation, our method reduces the requirements for annotation and still achieves a comparable performance. We also perform inferences on the training images and compare the results with the ground-truth annotations (Figure 4). Visual inspection shows that our method successfully learns from the annotated exemplars and propagates the partial annotations to the whole image.

E. Application

In this section, we show that our method can also be used as a computer-assisted annotating tool for creating fully annotated datasets. In brief, 20- μm -thick coronal sections of mouse brains were counterstained with DAPI and imaged with an LSM 780 confocal microscope (Carl Zeiss Microscopy). As shown in Figure 5, it is difficult to annotate all nuclei in these images because of the high nucleus density and ambiguous nuclei overlapping, but it is relatively easy and fast to perform partial annotating. We trained our network on 26 partially annotated images (second row of Figure 5) for 200 iterations. Then, we performed inferences on the same 26 images. As shown in the third row of Figure 5, our method can robustly learn from the labeled nucleus examples and propagate high-quality annotations to the whole image. We converted the

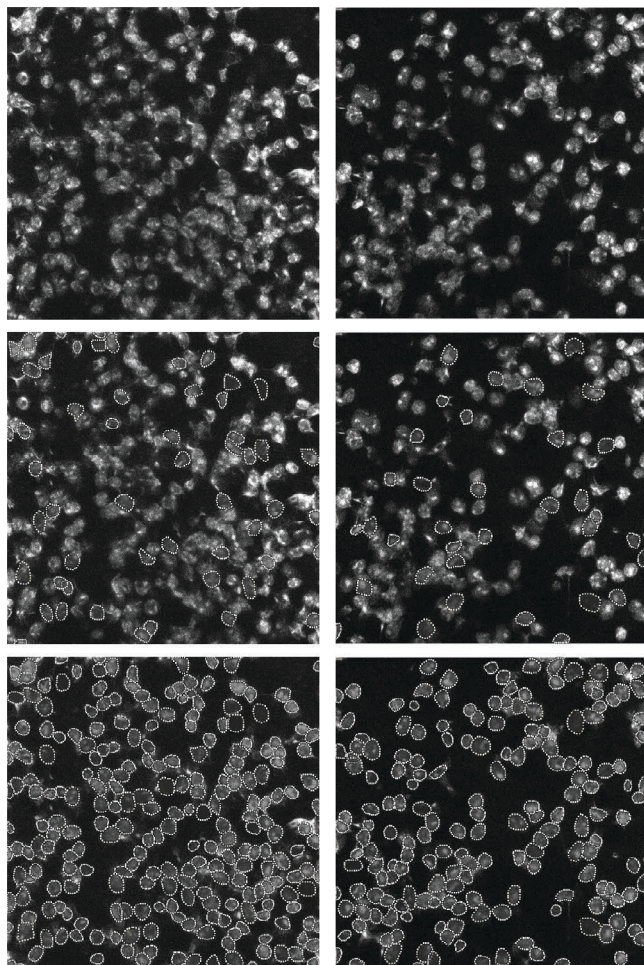


Fig. 5. Our method used as a computer-assisted annotating tool. The first row shows the example images to be annotated. The second row shows the partial annotations created by a human annotator. It is difficult for human annotators to annotate all nuclei in the images because of the high density and weak nuclei edges. The third row shows the annotations generated by our method after training. The generated annotations are presented as natural cubic splines with control points for further manual editing.

segmentation result into natural cubic splines with control points for further manual refinement.

IV. CONCLUSION

Automatic and reliable characterization of cells in images is key to many biological applications. Recently, deep learning-based segmentation frameworks have greatly improved segmentation performance and have achieved state-of-the-art results on many competitions. However, most of them require a fully annotated training dataset. It is often difficult to find compatible, public datasets with annotations because of the large variability in microscopy images [33]. In this work, we show that deep convolutional networks can capture the semantic similarity between nuclei in the same image by visualizing the self-attention map. Therefore, it is possible to extend the current frameworks to handle partially

annotated training data.

We propose a simple module to learn from a few exemplar annotations and then detect the potential unlabeled nuclei. We integrate this module into the Mask R-CNN framework and show that our proposed method can robustly learn from a partially labeled dataset. Our method uses fewer training data than its predecessor and achieves a comparable performance to the baseline method; therefore, it could greatly reduce the time needed for creating training datasets. The detection performance is slightly decreased when training with partial annotations because our network has fewer examples to learn from. One potential solution is to use data augmentation, which is not used in this work because it would complicate the analyses. However, it is difficult to find a good data augmentation strategy that will work well on different datasets [41]. Our method provides a better solution: when extreme segmentation accuracy is needed, our method can be used as a computer-assisted annotation tool to help create high-quality fully annotated training datasets.

It has been shown that when nuclei are correctly isolated, U-Net-based frameworks can generate better binary masks, probably because of the high-resolution features used in U-Net [32]. In this work, we performed nucleus prediction and regression on fpn1, whose spatial resolution (1/4) was lower than the image resolution. Problems may ensue if some of the nuclei to be detected are extremely small. In the future, our method could be extended to use some high-resolution networks [42] to further improve the detection and segmentation accuracy on nuclei with different sizes.

ACKNOWLEDGMENT

We thank Marcelo Cicconet, Neeraj Kumar, and Thomas Walter for providing the training datasets.

REFERENCES

- [1] N. Battich, T. Stoeger, and L. Pelkmans, "Control of Transcript Variability in Single Mammalian Cells," *Cell*, vol. 163, no. 7, pp. 1596–1610, 2015.
- [2] K. L. Frieda, J. M. Linton, S. Hormoz, J. Choi, K.-H. K. Chow, Z. S. Singer, M. W. Budde, M. B. Elowitz, and L. Cai, "Synthetic recording and in situ readout of lineage information in single cells," *Nature*, vol. 541, no. 7635, p. 107, 2017.
- [3] S. Shah, E. Lubeck, W. Zhou, and L. Cai, "In Situ Transcription Profiling of Single Cells Reveals Spatial Organization of Cells in the Mouse Hippocampus," *Neuron*, vol. 92, no. 2, pp. 342–357, 2016.
- [4] P. L. Ståhl, F. Salmén, S. Vickovic, A. Lundmark, J. Navarro, J. Magnusson, S. Giacomello, M. Asp, J. O. Westholm, M. Huss, A. Mollbrink, S. Linnarsson, S. Codeluppi, Å. Borg, F. Pontén, P. Costea, P. Sahlén, J. Mulder, O. Bergmann, J. Lundberg, and J. Frisén, "Visualization and analysis of gene expression in tissue sections by spatial transcriptomics," *Science*, vol. 353, no. 6294, pp. 78–82, 2016.
- [5] M. N. Gurcan, L. E. Boucheron, A. Can, A. Madabhushi, N. M. Rajpoot, and B. Yener, "Histopathological Image Analysis: A Review," *IEEE Rev Biomed Eng*, vol. 2, pp. 147–171, 2009.
- [6] N. Otsu, "A Threshold Selection Method from Gray-Level Histograms," *IEEE Transactions Syst Man Cybern*, vol. 9, no. 1, p. 62 66, 1979.
- [7] D. Bradley and G. Roth, "Adaptive Thresholding using the Integral Image," *J Graph Gpu Game Tools*, vol. 12, no. 2, pp. 13–21, 2007.
- [8] R. Bise and Y. Sato, "Cell Detection From Redundant Candidate Regions Under Nonoverlapping Constraints," *IEEE T Med Imaging*, vol. 34, no. 7, pp. 1417–1427, 2015.
- [9] C. Arteta, V. Lempitsky, A. J. Noble, and A. Zisserman, "Detecting overlapping instances in microscopy images using extremal region trees," *Med Image Anal*, vol. 27, no. C, pp. 3–16, 2016.
- [10] M. Liao, Y. Zhao, X. Li, P. Dai, X. Xu, J. Zhang, and B. Zou, "Automatic segmentation for cell images based on bottleneck detection and ellipse fitting," *Neurocomputing*, vol. 173, pp. 615–622, 2016.
- [11] X. Yang, H. Li, and X. Zhou, "Nuclei Segmentation Using Marker-Controlled Watershed, Tracking Using Mean-Shift, and Kalman Filter in Time-Lapse Microscopy," *IEEE Transactions Circuits Syst Regul Pap*, vol. 53, no. 11, pp. 2405–2414, 2006.
- [12] N. Malpica, C. de Solórzano, J. Vaquero, A. Santos, I. Vallcorba, J. García-Sagredo, and F. del Pozo, "Applying watershed algorithms to the segmentation of clustered nuclei," *Cytometry*, vol. 28, no. 4, pp. 289–297, 1997.
- [13] L. Nasser and T. Boudier, "A novel generic dictionary-based denoising method for improving noisy and densely packed nuclei segmentation in 3D time-lapse fluorescence microscopy images," *Sci Rep*, vol. 9, no. 1, p. 5654, 2019.
- [14] C. wählby, I. -M. Sinto, F. Erlandsson, G. Borgfors, and E. BENTGSSON, "Combining intensity, edge and shape information for 2D and 3D segmentation of cell nuclei in tissue sections," *J Microsc*, vol. 215, no. 1, pp. 67–76, 2004.
- [15] E. Türetken, X. Wang, C. J. Becker, C. Haubold, and P. Fua, "Network Flow Integer Programming to Track Elliptical Cells in Time-Lapse Sequences," *IEEE T Med Imaging*, vol. 36, no. 4, pp. 942–951, 2017.
- [16] M. Cicconet, D. Geiger, and K. Gunsalus, "Wavelet-based circular hough transform and its application in embryo development analysis," in *VISAPP 2013 - Proceedings of the International Conference on Computer Vision Theory and Applications*, 2013.
- [17] S. Akram, J. Kannala, L. Eklund, and J. Heikkilä, "Joint cell segmentation and tracking using cell proposals," in *IEEE 13th International Symposium on Biomedical Imaging (ISBI)*, pp. 920–924, 2016.
- [18] M. Schiegg, P. Hanslovsky, C. Haubold, U. Koethe, L. Hufnagel, and F. A. Hamprecht, "Graphical model for joint segmentation and tracking of multiple dividing cells," *Bioinformatics*, vol. 31, no. 6, pp. 948–956, 2015.
- [19] J. Funke, F. A. Hamprecht, and C. Zhang, "Learning to Segment: Training Hierarchical Segmentation under a Topological Loss," in *Medical Image Computing and Computer-Assisted Intervention – MICCAI 2015, 18th International Conference*, pp. 268–275, 2015.
- [20] K. Liu, S. S. Lienkamp, A. Shindo, J. B. Wallingford, G. Walz, and O. Ronneberger, "Optical Flow Guided Cell Segmentation and Tracking in Developing Tissue," in *IEEE International Symposium on Biomedical Imaging (ISBI)*, pp. 298–301, 2014.
- [21] G. J. Mohammed and T. Boudier, "Classified region growing for 3D segmentation of packed nuclei," in *IEEE International Symposium on Biomedical Imaging (ISBI)*, pp. 842–845, 2014.
- [22] S. Tonti, S. Cataldo, A. Bottino, and E. Ficarra, "An automated approach to the segmentation of HEp-2 cells for the indirect immunofluorescence ANA test," *Comput Med Imag Grap*, vol. 40, pp. 62–69, 2015.
- [23] J. C. Caicedo, J. Roth, A. Goodman, T. Becker, K. W. Karhohs, M. Broisin, M. Csaba, C. McQuin, S. Singh, F. Theis, and A. E. Carpenter, "Evaluation of Deep Learning Strategies for Nucleus Segmentation in Fluorescence Images," *Biorxiv*, p. 335216, 2019.
- [24] O. Ronneberger, P. Fischer, and T. Brox, "U-Net: Convolutional Networks for Biomedical Image Segmentation," in *Medical Image Computing and Computer-Assisted Intervention – MICCAI 2015, 18th International Conference*, pp. 234–241, 2015.
- [25] K. He, G. Gkioxari, P. Dollár, and R. Girshick, "Mask R-CNN," in *IEEE International Conference on Computer Vision (ICCV)*, 2017.
- [26] Kaggle, "2018 data science bowl," <https://www.kaggle.com/c/data-science-bowl-2018>, 2018.
- [27] D. Retina, "Deep Retina 3th place solution to Kaggle's 2018 Data Science Bowl," https://github.com/Lopezurrutia/DSB_2018, 2018.
- [28] ods.ai, "Dsb2018 [ods.ai] topcoders 1st place solution," https://github.com/selimsef/dsb2018_topcoders, 2018.
- [29] jacobkie, "2018 Data Science Bowl 2nd Place Solution," <https://github.com/jacobkie/2018DSB>, 2018.
- [30] H. Chen, X. Qi, L. Yu, Q. Dou, J. Qin, and P. Heng, "DCAN: Deep contour-aware networks for object instance segmentation from histology images," *Med Image Anal*, vol. 36, no. C, p. 135 146, 2017.
- [31] M. Cicconet, D. R. Hochbaum, D. L. Richmond, and B. L. Sabatini, "Bots for Software-Assisted Analysis of Image-Based Transcriptomics," in *IEEE International Conference on Computer Vision Workshops (ICCVW)*, pp. 134–142, 2017.

- [32] A. Vuola, S. Akram, and J. Kannala, "Mask-RCNN and U-net Ensembled for Nuclei Segmentation," in *IEEE International Symposium on Biomedical Imaging (ISBI)*, 2019.
- [33] P. Naylor, M. Lae, F. Reyat, and T. Walter, "Segmentation of Nuclei in Histopathology Images by Deep Regression of the Distance Map," *IEEE T Med Imaging*, vol. 38, no. 2, pp. 448–459, 2018.
- [34] X. Wang, R. Girshick, A. Gupta, and K. He, "Non-local Neural Networks," in *IEEE Conference on Computer Vision and Pattern Recognition (CVPR)*, 2018.
- [35] Z. Shen, M. Zhang, S. Yi, J. Yan, and H. Zhao, "Decomposed Attention: Self-Attention with Linear Complexities," *arXiv*, p. arXiv:1812.01243, 2018.
- [36] T.-Y. Lin, P. Dollár, R. Girshick, K. He, B. Hariharan, and S. Belongie, "Feature Pyramid Networks for Object Detection," in *IEEE Conference on Computer Vision and Pattern Recognition (CVPR)*, 2017.
- [37] R. Girshick, "Fast R-CNN," in *IEEE International Conference on Computer Vision (ICCV)*, 2015.
- [38] S. Xie, R. Girshick, P. Dollár, Z. Tu, and K. He, "Aggregated Residual Transformations for Deep Neural Networks," in *IEEE Conference on Computer Vision and Pattern Recognition (CVPR)*, 2017.
- [39] F. Massa and R. Girshick, "maskrcnn-benchmark: Fast, modular reference implementation of Instance Segmentation and Object Detection algorithms in PyTorch," <https://github.com/facebookresearch/maskrcnn-benchmark>, 2019.
- [40] N. Kumar, R. Verma, S. Sharma, S. Bhargava, A. Vahadane, and A. Sethi, "A Dataset and a Technique for Generalized Nuclear Segmentation for Computational Pathology," *IEEE T Med Imaging*, vol. 36, no. 7, pp. 1550–1560, 2017.
- [41] E. D. Cubuk, B. Zoph, D. Mane, V. Vasudevan, and Q. V. Le, "AutoAugment: Learning Augmentation Policies from Data," in *IEEE Conference on Computer Vision and Pattern Recognition (CVPR)*, 2019.
- [42] K. Sun, B. Xiao, D. Liu, and J. Wang, "Deep High-Resolution Representation Learning for Human Pose Estimation," in *IEEE Conference on Computer Vision and Pattern Recognition (CVPR)*, 2019.